ACS APPLIED MATERIALS & INTERFACES

RESEARCH ARTICLE

www.acsami.org

Transparent Large-Strain Thermoplastic Polyurethane Magnetoactive Nanocomposites

Mitra Yoonessi,[*,†,‡] John A. Peck,[§] Justin L. Bail,[†,‡] Richard B. Rogers,[‡] Bradley A. Lerch,[‡] and Michael A. Meador[‡]

[†]Ohio Aerospace Institute, Cleveland, Ohio
[‡]NASA Glenn Research Center, Cleveland, Ohio
[§]University of Akron, Akron, Ohio

ABSTRACT: Organically modified superparamagnetic $MnFe_2O_4$/thermoplastic polyurethane elastomer (TPU) nanocomposites (0.1−8 wt %) were prepared by solvent mixing followed by solution casting. Linear aliphatic alkyl chain modification of spherical $MnFe_2O_4$ provided compatibility with the TPU containing a butanediol extended polyester polyol-MDI. All $MnFe_2O_4$/TPU nanocomposite films were superparamagnetic and their saturation magnetization, σ_s, increased with increasing $MnFe_2O_4$ content. All nanocomposite films exhibited large deformations (>10 mm) under a magneto-static field. This is the first report of large actuation of magnetic nanoparticle nanocomposites at low-loading levels of 0.1 wt % (0.025 vol %). The maximum actuation deformation of the $MnFe_2O_4$/TPU nanocomposite films increased exponentially with increasing nanoparticle concentration. An empirical correlation between the maximum displacement, saturation magnetization, and magnetic nanoparticle loading is proposed. The cyclic deformation actuation of a 6 wt % surface modified $MnFe_2O_4$/TPU, in a low magnetic field $151 < B(y) < 303$ Oe, exhibited excellent reproducibility and controllability. $MnFe_2O_4$/TPU nanocomposite films (0.1−2 wt %) were transparent and semitransparent over the wavelengths from 350 to 700 nm.

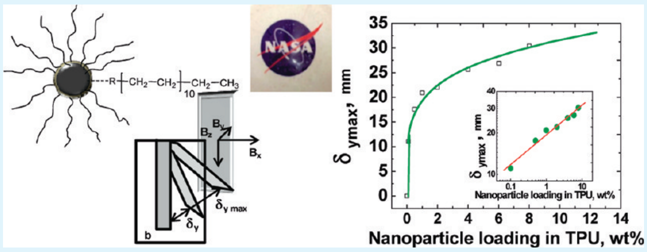

KEYWORDS: superparamagnetic nanoparticles, polymer actuator, magnetic polymer nanocomposite, magnetomechanical responsive polymers, adaptive nanocomposites, superparamagnetic shape memory films

INTRODUCTION

Polymer nanocomposite actuators are of great interest due to their potential applications in aerospace structural components,[1] microrobotics,[2] artificial muscles,[3] temperature-sensitive switches and valves,[4] and magnetodriven biocompatible devices.[5] Polymer nanocomposite actuators are materials that undergo mechanical deformation by the application of an external stimulus such as electrical field, electroresistive heating,[6,7] and ionic polymer metal composite,[8] thermal gradient,[9] light radiation,[10] and electrochemical media.[11,12] Electroresistive heating requires electrodes and wiring to the structural components. On the other hand, thermally activated shape memory polymers necessitate applying stress at a temperature above the switching temperature to fix the polymer shape after recovery. An alternative approach is the remote actuation of a magnetic polymer nanocomposite by a magnetostatic or electromagnetic field. This type of actuation results in deformation which is recoverable upon removal of the field, and is reproducible. This technology can be used for space deployable structures where a small compact, lightweight volume needs to undergo sudden large shape changes. It can also be extended to the actuation of structural components in aircraft, e.g., wings or fan blades where a magnetic field can induce deformation of components.

Magnetic actuation can be induced by applying a magnetic field (static or electromagnetic) to a magnetoactive polymer composite.[13−16] Magnetoactive polymer composites are hybrid materials composed of a polymer and magnetic material which exhibit overall magnetic properties. Magnetic nanoparticle polymer nanocomposites have great potential for large strain actuators because of their large particle number density, and the large interfacial area between the magnetic nanoparticles and the polymer matrix. Low loading levels of magnetic nanoparticles are important for aerospace applications since reduced weight is a critical driver for materials. Magnetic nanoparticles can be incorporated into soft polymer matrices to generate polymer nanocomposite actuators. This method can be extended to structural components with higher glass-transition temperatures to allow deformation above the glassy state.

Lightweight aerogel magnetic actuators prepared by freeze-dried cellulose nanofibril aerogels as templates for the nonagglomerated growth of cobalt-ferrite, have shown actuation responses even in low magnetic fields.[13] Coiling mechanisms and large deformations of spherical micrometer-sized iron particle

Received: April 14, 2011
Accepted: June 14, 2011
Published: June 28, 2011

dx.doi.org/10.1021/am200468t | ACS Appl. Mater. Interfaces 2011, 3, 2686–2693

polysiloxane have been reported for composites with particle loads of 20−77 wt %.[15] Reported magnetic actuation of iron oxide (γ-Fe_2O_3) nanorods in poly (lactide-*co*-glycolide) biocompatible nanocomposites (10−30 wt %) could potentially stimulate cells to promote nutrient supply.[5] Epoxy/micrometer-sized strontium ferrite powder composite (95.3 wt %) microactuators exhibited small deflections when tested both statically and dynamically.[14] Electromagnetic actuation of Ni nanowire/cellulose nanocomposites (∼34 wt %) with both DC and AC currents generating constant and alternating magnetic field have been reported.[16] Magnetic-sensitive gels of chemically cross-linked polymer networks with ∼10 nm monodomain magnetic nanoparticles undergo shape distortion when a magnetic field is applied.[17] The free energy of the swollen network containing both elastic and magnetic components has been studied as the basis for the shape change.[17] Nanocomposites of (3.5−6.5 nm) maghemite polystyrene exhibited structural supra-aggregate organization with a size of ∼200 nm at volume fractions, $\varphi \geq 5 \times 10^{-4}$. Here, primary aggregates were formed at lower volume fractions ($<5 \times 10^{-4}$) as shown by small-angle X-ray scattering and TEM.[18] The effects of magnetic nanoparticle addition on the thermal and mechanical properties of TPU have been reported.[19] The mechanical response of 1−10 wt % micrometer-sized Fe_3O_4/polyvinyl alcohol magnetic hydrogels in low magnetic field (400 Oe) has also been reported.[20]

Magnetic nanoparticles can be synthesized to generate different chemical compositions, shapes, sizes and aspect ratios.[21,22] These characteristics determine the magnetic strength of the nanoparticles.[21,22] Magnetic nanoparticles below a critical diameter are superparamagnetic, where the spin rotation is random, and the material can be magnetized and demagnetized upon application or removal of the magnetic field with no relaxation time.[21] These superparamagnetic nanoparticles have single domains and respond quickly to a magnetic field above the blocking temperature. They also tend to agglomerate because of magnetic, and van der Waals forces which lower the nanoparticles surface area. The high coercivity of superparamagnetic particles is attributed to single domain effects. The increase in the aspect ratio also results in a significant increase in coercivity, i.e., the coercivity of Fe nanoparticles increased from 820 to 10^4 Oe when the aspect ratio was increased from 1.1 to 10.[21] Magnetic nanoparticles have been synthesized by coprecipitation,[23,24] thermal decomposition,[25−27] microemulsion,[28,29] and hydrothermal synthesis.[30] Monodisperse metallic nanoparticles can be synthesized by a thermal decomposition method.[25−27] This method involves reduction of organometallic compounds in high boiling point solvents containing surfactants as a stabilizing agent and polyol as the reducing agent.[25−27]

This study reports on the preparation and characterization of surface-modified $MnFe_2O_4$/thermoplastic polyurethane elastomer nanocomposites (0.1−8 wt %) capable of large deformations under applied magnetic fields. Due to the small particle size of the superparamagnetic nanoparticles and low particle loading (0.1 and 0.5 wt %), the nanocomposites were transparent and exhibited large deformations in a static magnetic field.

EXPERIMENTAL METHODS

Materials. 1,2-Dodecanediol, lauric acid, dodecylamine, benzyl ether, and tetrahydrofuran (THF) were purchased from Sigma Aldrich. Iron(III) acetyl acetonate and manganese(II) acetyl acetonate were obtained from J.T. Baker Chemical Co. Thermoplastic polyurethane elastomer, TPU, Irogran 455−203, was generously donated by Huntsman Chemical Corp.

Synthesis of Magnetic Nanoparticles. Hydrocarbon-coated iron manganese oxide nanoparticles were synthesized using Sun's method.[25] Briefly, 2 mmol of iron(III) acetylactonate, 1 mmol of manganese acetyl acetonate, 6 mmol of dodecanoic acid, 10 mmol of 1,2 dodecanediol, and 6 mmol of dodecylamine were mixed with 20 cc of benzyl ether under a nitrogen blanket for 15 min. The reaction temperature was then increased to 150 °C for 30 min and subsequently to ∼300 °C for an additional 30 min. The iron manganese oxide nanoparticles were precipitated in methanol after cooling, and then centrifuged and washed several times with excess methanol.

Nanocomposite Film Preparation. Magnetic nanoparticles were dispersed in THF and sonicated for 5 min to generate visibly aggregate free dispersions. TPU was dissolved in THF, and then mixed with surface-modified $MnFe_2O_4$/THF suspensions. These TPU/surface-modified $MnFe_2O_4$/THF dispersions were sonicated for 30 min and then solvent cast to generate 75−100 μm thick nanocomposite films (0.1−8 wt %). The films were dried in a vacuum oven to remove excess solvent. Weight percentages of the nanocomposites were calculated on the basis of $MnFe_2O_4$ content.

Characterizations. A Q500TGA Thermogravimetric analyzer was used under nitrogen from 25 to 800 °C with a scan rate of 10 °C/min. FT-IR spectra were obtained using a Nicolet 380 Fourier transform infrared spectrometer. High resolution transmission electron microscopy (HR-TEM) of the nanoparticles was performed using a Philips CM200 instrument. Scanning electron microscopy was performed using a FEG-SEM Hitachi. The cryo-fractured surfaces were exposed to air plasma for 3 min before examination by FE-SEM. Wide angle X-ray scattering (WAXS) was performed on a Bruker D8 advance X-ray diffractometer configured in the Bragg−Brentano geometry with Cu Kα ($\lambda = 1.5418$ Å) radiation source and a linear position sensitive detector.

AC Field Gradient Magnetometer. Magnetic hysteresis data were collected using a Princeton Measurements Corporation, Alternating Gradient Magnetometer (AGM) Model 2900. After DC demagnetization of the samples, the magnetic hysteresis loop was generated resulting in a magnetic field between ±14,000 Oe. From the hysteresis loop the magnetic saturation (σ_s), coercive force (H_c) and saturation remanent magnetization (σ_{rs}) were determined. To determine the coercivity of remanence (H_{cr}), we saturated the sample at 14 000 Oe and then incrementally larger reversed fields were applied, switched-off and followed by measurement of sample remanent magnetization.

Magnetomechanical Testing. Magnetomechanical testing was performed on a microload, pneumatic test rig. Tests were performed in stroke control at a rate of 0.5 mm/s. Full-field optical displacement imaging was used with a frame capture rate of 0.125 s. A typical nanocomposite film sample size of ∼36 ± 1 (mm) × 26 ± 0.5 (mm) × 0.1 ± 0.03 (mm) was placed vertically at a starting distance of 50 mm from the magnet. A static magnet with a strength of 4300 Oe (B_y ($y = 0$)) was used. All three components of the magnetic field were measured by a triple-axis magnetometer. Only B_y is acting on the film surface perpendicular to the x−z plane (B_x and B_z were negligible and verified by the measurements). The z-variation of B_y was negligible along the film z-axis within the experimental geometry constraints. The sample was moved toward the magnet using the test rig stroke, and this resulted in the increasing magnetic field. The magnetic field, B_y, variations with the position along the y direction was measured in 0.5 mm increments and fit to a sixth order polynomial. Deflection of the film, δ_y, was monitored using the optical displacement system.

RESULTS AND DISCUSSIONS

Magnetic Nanoparticle Characterization. Surface modification of iron manganese oxide nanoparticles is essential to provide compatibility between the nanoparticles and the thermoplastic polyurethane elastomer matrix. Absence of surface modifier results in poor dispersion and aggregation of metallic oxide nanoparticles within the organic polymer matrix. This will lead to poor mechanical properties and actuation performance. The magnetic nanoparticle synthesis method used in this study resulted in iron manganese oxide nanoparticles with an organic modifier corona on the surface. The TGA of the surface-modified $MnFe_2O_4$ nanoparticles shows ~29 wt % hydrocarbon on the surface of the $MnFe_2O_4$ nanoparticles with a degradation temperature onset of 190 °C, and a maximum degradation temperature of 291.2 °C (Figure 1).

The FT-IR spectrum of the organic surface modifier exhibited a band at 3337.1 cm^{-1} corresponding to −OH stretch possibly due to 1,2 dodecanediol, or the presence of a hydroxyl group on the $MnFe_2O_4$ surface (Figure 2). The −CH stretch of saturated aliphatic hydrocarbons generally appears in the range of 3000 to 2800 cm^{-1}, whereas the bending appears at 1500 and 1300 cm^{-1}.[31] The stretches observed at 2922.5 and 2852.6 cm^{-1} are due to the −CH stretch in $C-CH_3$, and to the $-CH_2$ presence in the aliphatic hydrocarbon chain of the organic modifiers (Figure 2). The absorption peaks observed at 1430.8 and 1556.6 cm^{-1} are characteristic of the −CH bending stretches.

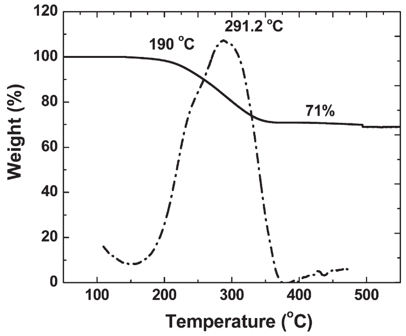

Figure 1. Weight loss versus temperature for organically modified $MnFe_2O_4$ nanoparticles exhibits 29% organic content (solid line). Weight loss derivative versus temperature showing a maxima at 291.2 °C (dashed line).

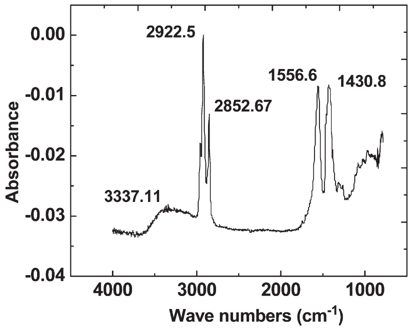

Figure 2. Infrared spectra of the surface-modified $MnFe_2O_4$ nanoparticles.

Figure 3a shows the TEM micrograph of the organically modified $MnFe_2O_4$ nanoparticles. The observed separation between the nanoparticles is attributed to the organic surface modifier on the $MnFe_2O_4$ nanoparticles. High-resolution imaging showed the presence of nearly uniform spherical nanoparticles with an average diameter of 6.11 ± 0.69 nm (Figure 3b) measured among 250 nanoparticles. This is in excellent agreement with the expected average diameter range reported for this synthesis method.[25] Figure 3c shows the electron diffraction pattern of the organically modified $MnFe_2O_4$ nanoparticles where the diffraction pattern corresponding to *hkl* indices of 220, 311, 400, 422, 511 are identified.

Lattice spacing and the crystalline structure of the organically modified iron manganese oxide nanoparticles were studied using WAXS (Figure 4). The diffraction peaks from the WAXS spectrum show an excellent match to the relative *hkl* indices of $MnFe_2O_4$ in the PDF database.[32] Table 1 lists calculated *d*-spacing based on the relative diffraction peaks of the bulk WAXS spectra of synthesized $MnFe_2O_4$ nanoparticles and their matched *hkl* indices.

A material's magnetic characteristic depends on its chemical composition, size, and aspect ratio.[21,22,33] $MnFe_2O_4$ has a Curie temperature, T_c, of 300 °C and is superparamagnetic at diameters at least up to 9.9 nm.[34] The magnetic properties of the surface-modified $MnFe_2O_4$ nanoparticles were measured using an alternating-field gradient magnetometer and, because of their small size, exhibited closed-loop, superparamagnetic behavior (Figure 5). The magnetization of a permanent magnet after removal of the external magnetic field is called remanence.[21,22,33] The saturation magnetization, σ_s, is the magnetic moment of elementary atoms per unit weight where all of the dipoles are aligned parallel. The reverse magnetic field required to reduce a materials magnetization to zero while the sample is in the magnetic field is called coercivity, H_c. The surface-modified $MnFe_2O_4$ nanoparticles have a saturation magnetization, σ_s, of 33.73 emu/g, a remanent magnetization of 0.125 emu/g, a coercivity, H_c, of 5.93 Oe and a coercivity of remanence, H_{cr}, of 46 Oe.

Nanocomposite Characterization. Thermoplastic polyurethane (TPU) elastomers have been widely used as stimuli-responsive polymers due to their segregated two-phase structure as first discovered by Mitsubishi in 1988.[35] TPU consists of hard

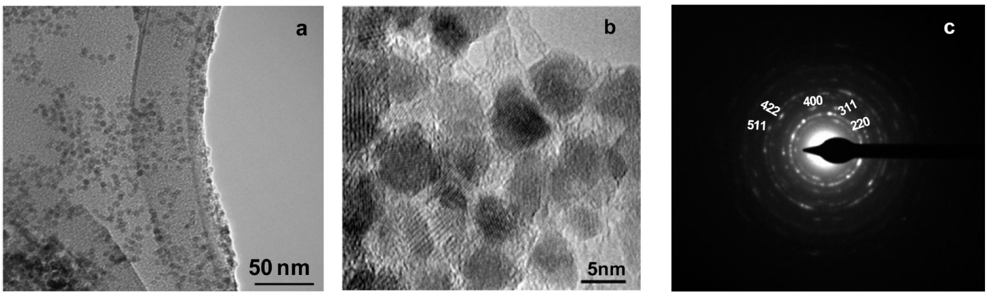

Figure 3. (a) TEM micrograph of surface-modified $MnFe_2O_4$ nanoparticles. (b) High-resolution micrographs of the same $MnFe_2O_4$ nanoparticles. (c) Electron microdiffraction pattern of the $MnFe_2O_4$ nanoparticles.

and soft segments and a chain extender and has a tunable glass transition temperature and mechanical properties. Soft segments could crystallize and act as physical cross-links enabling shape recovery effects.[36,37] TPU used in this study was synthesized by polycondensation reaction of 4-4′methylenediphenylene isocyanate (MDI) and polyol using butanediol as chain extender.[35] Its microstructure is reported to consist of 9.9% hard segments, 58.2% butanediol chain extenders, and 31.8% adipate soft segments.[36] It has shown thermal shape memory effects when used as a host matrix for zinc nanorods and multiwall nanotubes.[36,37]

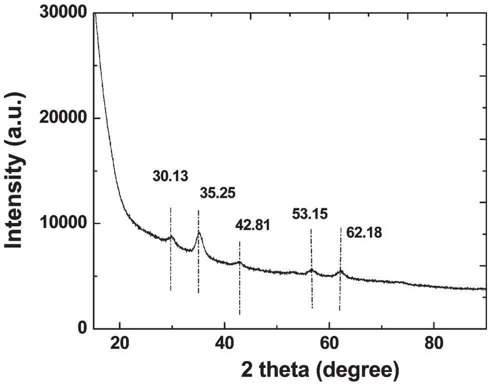

Figure 4. WAXS of the surface-modified $MnFe_2O_4$ nanoparticles.

Table 1. Measured Lattice Spacing, *d* (Å), Based on the Diffraction Peaks of WAXS Spectra along with *hkl* Matched with PDF Database

	WAXS diffraction peaks						
	1	2	3	4	5	6	7
d	2.96	2.54	2.11	1.72	1.62	1.49	1.27
$MnFe_2O_4$	2.97	2.54	2.10	1.72	1.62	1.49	1.27
hkl	220	311	400	422	511	440	622

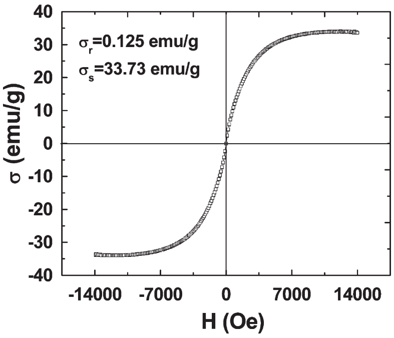

Figure 5. Magnetization vs magnetic field for the surface-modified $MnFe_2O_4$ nanoparticles reveals a superparamagnetic closed loop.

The surface-modified $MnFe_2O_4$ nanoparticles were dispersed in TPU containing soft segments of an aliphatic alkyl chain to generate nanocomposites films. The chemical architecture of the TPU and a schematic of the organically modified $MnFe_2O_4$ nanoparticles are shown in Figure 6. A stable dispersion of organically modified $MnFe_2O_4$ nanoparticles in THF was obtained (Figure 6c) which was then mixed with a solution of TPU in THF to generate the nanocomposites films.

The presence of long-chain aliphatic hydrocarbons promotes the compatibility between the inorganic $MnFe_2O_4$ nanoparticle and the polyurethane due to the presence of aliphatic hydrocarbon moieties in the polyurethane polymer chains. This will improve the dispersion of the $MnFe_2O_4$ nanoparticles within the TPU polymer matrix. The surface-modified $MnFe_2O_4$/TPU nanocomposite films were prepared with particle loadings of 0.1, 0.5, 1, 2, 4, 6, and 8 wt % (0.025, 0.126, 0.252, 0.51, 1.03, 1.57, 2.13 vol %), based on the weight/volume of the metallic core ($\rho_{MnFe2O4}$ = 4.76 g/cm^3 and ρ_{TPU} = 1.19 g/cm^3). The low weight/volume particle loadings of the nanocomposites were critical in achieving overall lightweight nanocomposites.

Nanocomposite Film Morphology. *TEM.* The dispersion of 2 wt % surface-modified $MnFe_2O_4$ nanoparticles in the TPU nanocomposite film was examined by TEM after cryo-microtoming of the film. A variety of nanoparticle clusters, ranging from a few nanoparticles, to larger nanoscale clusters, and micrometer-sized aggregates was observed (Figure 7). Magnetic and van der Waals attractive forces result in aggregation of the nanoparticles within the film. Dispersion of 4 nm maghemite (γ-Fe_2O_3) nanoparticles in polystyrene occurred only at loading levels below 0.01 vol % whereas, 200 nm supra-aggregates occurred at loading levels above 0.05 vol %.[18]

SEM. Images a and b in Figure 8 show the SEM backscatter micrographs of the 0.5 and 6 wt % surface-modified $MnFe_2O_4$/TPU nanocomposite films after treatment with an oxygen plasma. The more dense $MnFe_2O_4$ nanoparticle aggregates appear as bright areas on the SEM micrographs. The aggregate size ranges between 1 and 3 micrometers (average of 1.7 μm) for 0.5 wt % and 1.1−2.9 μm (average of 2 μm) for 6 wt % $MnFe_2O_4$-loaded films. The nanometer-size magnetic nanoparticles and clusters are not resolved at this SEM magnification. The film containing 6 wt % surface-modified $MnFe_2O_4$ nanoparticles exhibited increased nanoparticle density on one side indicating settling of the heavier $MnFe_2O_4$ nanoparticles during solvent evaporation (Figure 8b). This settling effect was not observed for 0.5, 1, 2, or 4 wt % surface-modified $MnFe_2O_4$/TPU. However, settling was more significant for 8 wt % surface-modified $MnFe_2O_4$/TPU nanocomposite film.

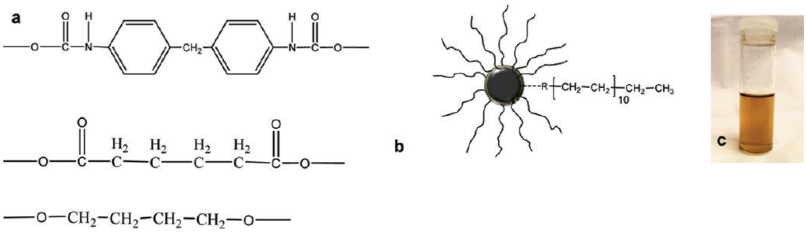

Figure 6. (a) Chemical structure and composition of the TPU, MDI, butanediol and polyol. (b) Schematics of surface-modified $MnFe_2O_4$ nanoparticles. (c) Dispersion of surface-modified $MnFe_2O_4$ nanoparticles in THF.

Optical and Magnetic Properties. The transparency of the surface-modified $MnFe_2O_4$/TPU nanocomposite films was measured over a wavelength range of 400−700 nm with UV−vis (Figure 9a). The neat TPU film showed a transmission of 97−90% in the range of 700−550 nm, while dropping from 90% to 74.4%, between 550 and 400 nm range. The transmission of the 0.1 wt % nanocomposite films was comparable with the neat TPU film where a slight decrease in transmission was observed from 400 to 460 nm. The decrease in transmission of the 0.5 wt % surface modified $MnFe_2O_4$/TPU nanocomposite in the 700−550 nm range was 91 to 75%, and 75 to 49.5% for the wavelength range of 550−400 nm. Further increase in the loadings of the surface-modified $MnFe_2O_4$ to 1 wt % resulted in a decrease in transmission from 73 to 42% for the wavelength range of 700−550 nm, and a further decrease of 42−20% for the wavelength range of 550−400 nm. The TPU nanocomposite containing 2 wt % surface-modified $MnFe_2O_4$ did not show a significant transmission decrease in the range of 700−550 nm range and had a transmission of 69.35 to 33%. However, the transmission in the range of 550−492 nm significantly dropped from 33 to 20% and below 10% for the wavelengths below 470 nm. The 4 wt % surface-modified $MnFe_2O_4$/TPU exhibited a transmission of 53.6 to 16.7% in the range of 700−610 nm with a sharp drop to below 10% of wavelengths shorter than 590 nm. The TPU/surface-modified $MnFe_2O_4$ nanocomposite with particle loadings of 0.1 and 0.5 wt % were transparent, 1 and 2 wt % were semitransparent, and 4 wt % was opaque.

Magnetization of the surface-modified $MnFe_2O_4$/TPU nanocomposites was measured to provide information about saturation magnetization, and coercivity. The coercivity of all surface-modified $MnFe_2O_4$ /TPU nanocomposite films was in the range of 8 ± 1 Oe. Figure 10 shows the saturation magnetization, σ_s, of the nanocomposite films versus concentration of the $MnFe_2O_4$ nanoparticles. The normalization of the magnetic moment versus magnetic field was performed based on the total weight of the nanocomposite film (TPU + surface modified $MnFe_2O_4$). The plot of saturation magnetization of the nanocomposite films versus magnetic nanoparticle concentration shows an exponential trend as follows

$$\sigma_s = A\omega^B \qquad (1)$$

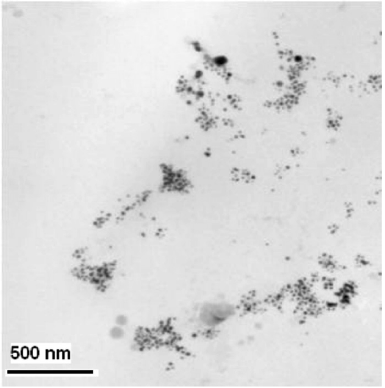

Figure 7. High-resolution TEM micrograph of the 2 wt % surface-modified $MnFe_2O_4$ TPU nanocomposite film.

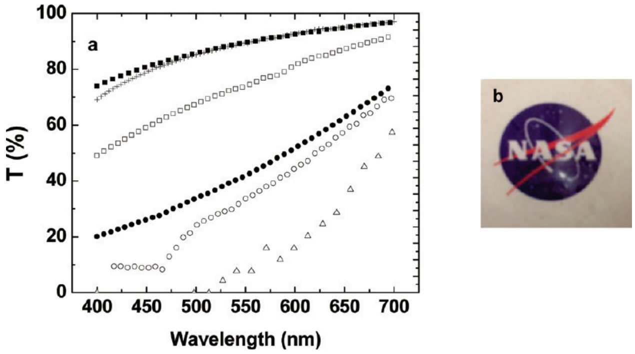

Figure 9. (a) Transmission of visible light (wavelengths of 400−700 nm) through TPU neat film (■), 0.1 wt % (+), 0.5 wt % (□), 1 wt % (●), 2 wt % (○), and 4 wt % (Δ) surface-modified $MnFe_2O_4$/TPU nanocomposite films. (b) Transparent 0.1 wt % surface modified $MnFe_2O_4$/TPU nanocomposite film in front of NASA logo.

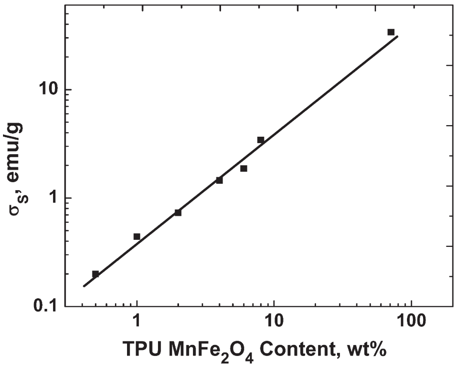

Figure 10. Exponential dependence of saturation magnetization versus $MnFe_2O_4$ weight percent in the TPU/nanocomposite films.

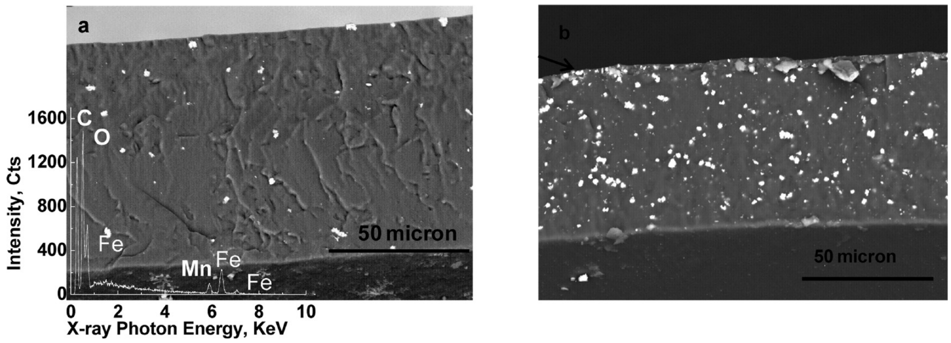

Figure 8. Bright-field SEM micrographs of oxygen plasma-treated cryo-fractured (a) 0.5 and (b) 6 wt % $MnFe_2O_4$ in the TPU matrix.

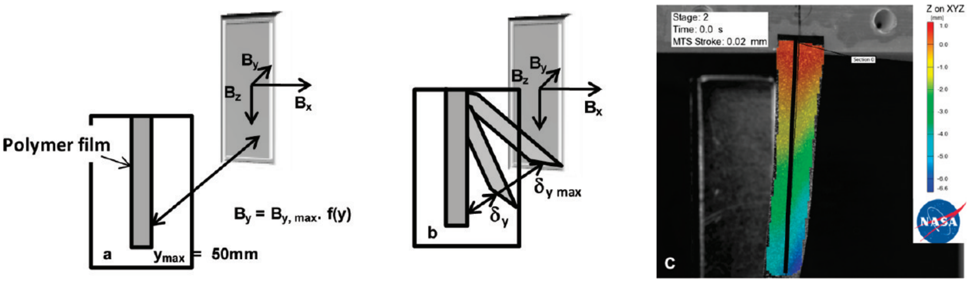

Figure 11. Schematics of (a) nanocomposite film positioning with respect to the magnetic field. (b) Film displacement, δ_y, and maximum displacement, δ_{ymax} in the magnetic field. (c) Measured and calculated y displacement (δ_y) of the 8 wt % surface-modified $MnFe_2O_4$ in the static magnetic field.

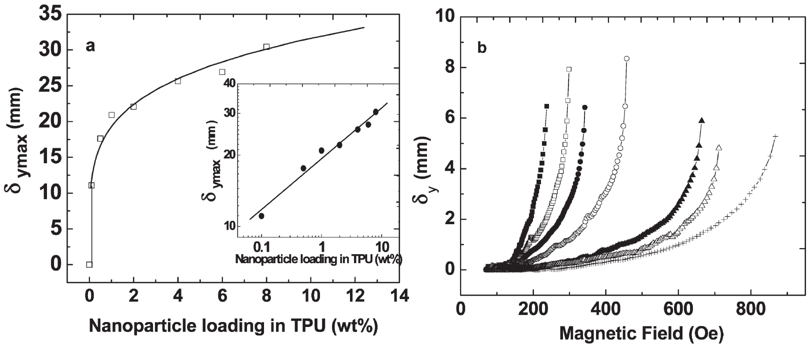

Figure 12. (a) Maximum displacement (δ_{ymax}) vs surface-modified $MnFe_2O_4$ loading in TPU polymer matrix (0.1−8 wt %). (b) Nanocomposite (0.1−8 wt %) film displacements plotted against magnetic field. (+) 0.1, (△) 0.5, (▲) 1, (○) 2, (●) 4, (□) 6, and (■) 8 wt % surface-modified $MnFe_2O_4$/TPU nanocomposites.

where A is 380.2 ± 0.033 and B is 1.02 ± 0.038 with $r^2 = 0.99$.

It should be noted that, the magnetic moment versus magnetic field was also normalized with respect to the weight of the magnetic nanoparticles contained in each nanocomposite film. This normalization yielded constant values for coercivity, H_c, 8 ± 1 Oe and magnetization saturation, σ_s, $(4 \pm 1) \times 10^{-5}$ emu/g.

Magnetomechanical Characterization. The nanocomposite films have magnetic characteristics that result from the embedded superparamagnetic $MnFe_2O_4$ nanoparticles. These films were placed in a static magnetic field, $\vec{H}$, where a magnetic force, $\vec{F}$, is applied that is proportional to the magnetic potential, $\vec{U}$. The magnetic moment, $\vec{M}$, is related to the magnetic field, $\vec{H}$ (maximum value of H_0), with a susceptibility, χ.[33] The force acting on the volume of a magnetic material depends on the magnetic field moment and the rate of the magnetic field change in that direction, where V is the volume.

$$\frac{d\,\vec{M}}{d\,\vec{H}} = \chi \tag{2}$$

$$\vec{U} = \int_0^{H_0} \vec{M} d\,\vec{H} \tag{3}$$

$$\vec{U} = \frac{1}{2}\chi H_0 \tag{4}$$

$$\vec{F} = -\vec{\nabla}\,\vec{U} \tag{5}$$

$$F_y = M_y \int_0^V \frac{dH_y}{dy} dV \tag{6}$$

The displacement of the magnetic film (δ) is determined using the static deflection of a cantilever beam, where I is moment of inertia, L, W, and b are length, width and thickness, respectively.

$$\delta = \frac{F_y L^3}{3EI} \tag{7}$$

$$I = bW^{3/12} \tag{8}$$

The magnetic field was induced by a static magnet with a magnetic field of B_y $(y = 0) = 4300$ Oe corresponding to the onset of saturation magnetization for the nanoparticles. Figures 11a and b show a schematic of the film position with respect to the magneto-static field. The test begins with the film positioned 50 mm from the magnet. The film is then moved toward the magnet at a rate of 0.5 mm/s using the test frame. Once the film is in close proximity of the magnet, the magnetic field causes the film to move gradually in the y direction. This deflection is measured using the optical displacement equipment and is given as displacement, δ_y, for various points along the length of the film. Figure 11c shows the color-coded displacement in the y-direction (out of the plane of the photo) for the 8 wt % surface-modified $MnFe_2O_4$ film in the magnetic field.

Upon approaching the magnet, the film moves gradually in the y direction where one end is fixed. However, the film eventually reaches a point where the magnetic force applied on the film is equal to the weight and the force required for the maximum deformation resulting in complete pulling of the film to the magnet. The separation distance at this point was the maximum displacement, δ_{ymax}.

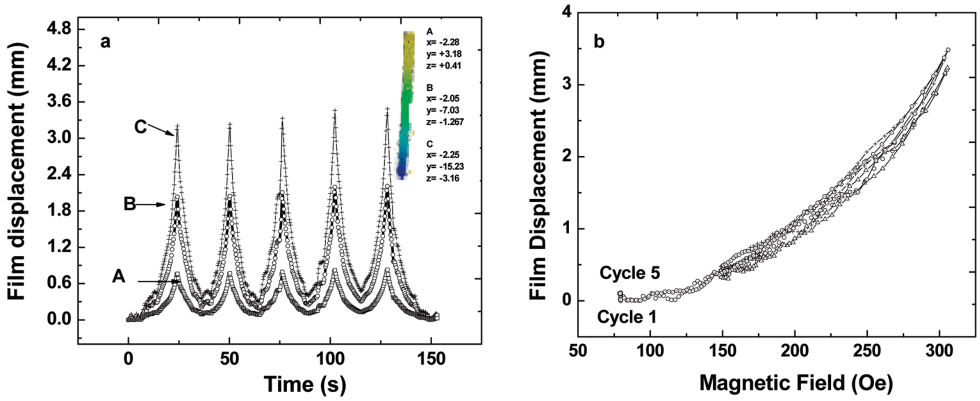

Figure 13. (a) Film displacement of the 6 wt % magnetic nanoparticle nanocomposite versus time spanning five cycles. The data were obtained at three points, A (□), B (○), and C (+) along the length of the film (*z* axis). (b) Film displacement of the same nanocomposite in 5 cycles versus magnetic field.

Figure 12 depicts the maximum displacement, δ_{ymax}, versus loading of the magnetic nanoparticles. The maximum displacement exhibits an exponential decay with the following fitting parameters

$$\delta_{ymax} = A\omega^{B} \tag{9}$$

where $A = 19.28 \pm 0.01$, $B = 0.21 \pm 0.015$ with $r^2 = 0.99$.

Combining eq 9 with eq 1, an empirical equation correlating the maximum displacement, δ_{ymax}, to the film saturation magnetization, σ_s, and magnetic nanoparticle weight percent can be proposed

$$\delta_{ymax} = 0.5\sigma_s\omega^{-0.81} \tag{10}$$

This correlation suggests that the maximum displacement has a stronger dependence on the saturation magnetization than on the weight percent of the magnetic nanoparticles.

The maximum displacement increased significantly with increasing magnetic nanoparticle concentration particularly at low particle loadings of up to 2 wt % (Figure 12a). As expected, the nanocomposites containing more than 2 wt % reached their maximum deformation at even greater distances. For example, the maximum displacement for the 0.1 wt % (0.025 vol %) nanocomposite is 11.1 mm whereas the maximum displacement for the 8 wt % (2.13 vol %) nanocomposite is 30.42 mm. It is evident that surface-modified $MnFe_2O_4$/TPU nanocomposites exhibit large displacements even with a low particle load of 0.1 wt % (0.025 vol %). This is the first known report of large actuation for magnetic nanoparticle nanocomposites having low particle loadings of 0.1 wt %.

Figure 12b shows the displacement of the surface modified $MnFe_2O_4$/TPU nanocomposites versus applied magnetic field. The displacement rate is lower for films containing low particle loads, and increases as the particle loading increases.

Because accurate control over actuation is critical to actuator performance, the recovery and response time of the films were examined. Cyclic deformation of the nanocomposite film containing 6 wt % $MnFe_2O_4$ nanoparticle loading was performed five times in a low magnetic field of 151 (Oe) < $B(y)$ < 303 (Oe). Figure 13a shows the film displacement versus time while cycling in the magnetic field. The imposed cyclic period time was 25 s with the film having an approximate 3 s lag time. The maximum displacement of the films from cycle-to-cycle was constant and reproducible within the experimental conditions. The films also returned to their original position as the cycle returned to the low value of the magnetic field.

To determine the loss and hysteresis of the 6 wt % nanocomposite film in the magnetic field (151 Oe < $B(y)$ < 303 Oe) the film displacement is plotted in Figure 13b for all five cycles. The traces from all five cycles were identical within experimental error. Neither hysteresis nor permanent deformation could be discerned from this test.

■ CONCLUSIONS

Surface modified $MnFe_2O_4$/TPU nanocomposite films with nanoparticle loading between 0.1 and 8 wt % were prepared by solution mixing followed by solvent casting. All of the films exhibited superparamagnetic behavior and the saturation magnetization increased with increasing nanoparticle content. Nanocomposite films were transparent or semitransparent when the surface modified $MnFe_2O_4$ nanoparticle loading was less than 2 wt %. Films with nanoparticle loadings of 4 wt % and higher were opaque. Large displacements (>10 mm) of all magnetic nanocomposite films were observed when a static magnetic field was applied. This is the first report of large actuation of magnetic nanoparticle nanocomposites with low loading magnetic nanoparticle levels of 0.1 wt % (0.025 vol %). The maximum displacement increased with increasing magnetic nanoparticle content. The proposed empirical correlation between the maximum displacement, saturation magnetization, and magnetic nanoparticle loading suggests a linear dependence of the maximum displacement to the saturation magnetization and a correlation to the nanoparticle weight percentage. TEM and SEM micrographs show variable dispersion ranging from small nanometer-sized clusters to more abundant micrometer-sized aggregates.

■ AUTHOR INFORMATION

Corresponding Author

*E-mail: mitra.yoonessi@nasa.gov.

■ ACKNOWLEDGMENT

The NASA Aeronautics-Subsonic Fixed Wing Program (Contract NNC07BA13B) provided financial support for this work. Thanks go to Charles Rosenblatt of Case Western Reserve for his helpful discussions. The cryo-microtoming of JoAn

Hudson of Clemson University is also greatly appreciated. Dave Hull, Terry McCue, and Daniel Scheiman of NASA-GRC and ASRC are greatly acknowledged for their lab support.

■ REFERENCES

(1) Crawley, E. F. *AIAA J.* **1994**, *32*, 1689–1699.

(2) Kim, B.; Kim, D.-H.; Jung, J.; Park, J.-O. *Smart Mater. Struct.* **2005**, *14*, 1579–1585.

(3) Fuhrer, R.; Athanassiou, E. K.; Luechinger, N. A.; Stark, W. J. *Small* **2009**, *5*, 383–388.

(4) Richter, A.; Kuckling, D.; Howitz, S.; Gehring, T.; Arndt, K.-F. *IEEE J. Microelectromech. Syst.* **2003**, *12*, 748–753.

(5) Mack, J. J.; Cox, B. N.; Lee, M.; Dunn, J. C.Y.; Wu, B. W. *J. Mater. Sci.* **2007**, *42*, 6139–6147.

(6) Sellinger, A. T.; Wang, D. H.; Tan, L.-S.; Vaia, R. A. *Adv. Mater.* **2010**, *22*, 3430–3435.

(7) Gunes, I. S.; Jimenez, G. A.; Jana, S. C. *Carbon* **2009**, *47*, 981–997.

(8) Shahinpoor, M. *Electrochim. Acta* **2003**, *48*, 2343–2353.

(9) Behl, M.; Lendlein, A. *Mater. Today* **2007**, *10*, 20–28.

(10) Ahir, S. V.; Terentjev, E. M. *Nat. Mater.* **2005**, *4*, 491–495.

(11) Xie, X.; Qu, L.; Zhou, C.; Li, Y.; Zhu, J.; Bai, H.; Shi, G.; Dai, L. *ACS Nano* **2010**, *9*, 6050–6054.

(12) Gu, G.; Schmid, M.; Chiu, P.-W.; Minett, A.; Fraysse, J.; Kim, G.-T.; Roth, S.; Kozlov, M.; Munoz, E.; Baughman, R. H. *Nat. Mater.* **2003**, *2*, 316–319.

(13) Olsson, R. T.; Azizi Samir, M. A. S.; Salazar-Alvarez, G.; Belova, L.; Ström, V.; Berglund, L. A.; Ikkala, O.; Nogués, J.; Gedde, U. W. *Nat. Nanotechnol.* **2010**, *5*, 584–588.

(14) Lagorce, L. K.; Brand, O.; Allen, M. G. *IEE J. Microelectromech. Syst.* **1999**, *8* (1), 2–9.

(15) Nguyen, V. Q.; Ramanujan, R. V. *Macromol. Chem. Physic.* **2010**, *211*, 618–626.

(16) Park, J.-M.; Kim, S.-J.; Jang, J.-H.; Wang, Z.; Kim, P.-G.; Yoon, D.-J.; Kim, J.; Hansen, G., K.; DeVries, L. *Compos., Part B* **2008**, *39*, 1161–1169.

(17) Szabo, D.; Szeghy, G.; Zrinyi, M. *Macromolecules* **1998**, *31*, 6541–6548.

(18) Robbes, A.-S.; Jestin, J.; Meneau, F.; Dalmas, F.; Sandre, O.; Perez, J.; Bou, F.; Cousin, F. *Macromolecules* **2010**, *43*, 5785–5796.

(19) Ashjari, M.; Mahdavian, A. R.; Golshan Ebrahimi, N.; Mosleh, Y. *J. Inorg. Organomet. Polym.* **2010**, *20*, 213–219.

(20) Ramanujan, R. V.; Lao, L. L. *Smart Mater. Struct.* **2006**, *15*, 952–956.

(21) Lu, A.-H.; Salabas, E. L.; Schuth, F. *Angew Chem., Int. Ed.* **2007**, *46*, 1222–1244.

(22) Leslie-Pelecky, D. L.; Rieke, R. D. *Chem. Mater.* **1996**, *8*, 1770–1783.

(23) Bee, A.; Massart, R.; Neveu, S. *J. Magn. Magn. Mater.* **1995**, *149*, 6–9.

(24) Cushing, B. L.; Kolesnichenko, V. L.; Connor, C. J. O. *Chem. Rev.* **2004**, *104*, 3893–3946.

(25) Sun, S.; Zeng, H.; Robinson, D. B.; Raoux, S.; Rice, P. M.; Wang, S. X.; Li, G. *J. Am. Chem. Soc.* **2004**, *126*, 273–279.

(26) Murray, C. B.; Norris, D. J.; Bawendi, M. G. *J. Am. Chem. Soc.* **1993**, *115*, 8706–8715.

(27) Brien, S. O; Brus, L.; Murray, C. B. *J. Am. Chem. Soc.* **2001**, *123*, 12085–12086.

(28) Destrée, C.; Nagy, J. B. *Adv. Colloid Interface Sci.* **2006**, *123−126*, 353–367.

(29) Carpenter, E. E.; Seip, C. T.; Connor, C. J. O. *J. Appl. Phys.* **1999**, *85*, 5184–5186.

(30) Wang, X.; Zhuang, J.; Peng, Q.; Li, Y. *Nature* **2005**, *437*, 121–124.

(31) Coates, J. Interpretation of Infrared Spectra, A Practical Approach. In *Encyclopedia of Analytical Chemistry*; Meyers, R. A., Ed.; John Wiley & Sons: New York, 2000; pp 10815−10837.

(32) Cornell, R. M., Schwertmann, U. *The Iron Oxides: Structure, Properties, Reactions, Occurrence and Uses*; VCH: New York, 1996; pp 167−168.

(33) Jiles, D., *Introduction to Magnetism and Magnetic Materials*; Chapman & Hall/CRC: Boca Raton, FL, 1991.

(34) Masala, O.; Seshadri, R. *Chem. Phys. Lett.* **2005**, *402*, 160–164.

(35) Lee, B. S.; Chun, B. C.; Chung, Y.-C.; Sul, K. I.; Cho, J. W. *Macromolecules* **2001**, *34*, 6431–6437.

(36) Koerner, H.; Kelley, J.; George, J.; Drummy, L.; Mirau, P.; Bell, N. S.; Hsu, J.W. P.; Vaia, R. A. *Macromolecules* **2009**, *42*, 8933–8942.

(37) Koerner, H.; Price, G.; Pearce, N. A.; Alexander, M.; Vaia, R. A. *Nat. Mater.* **2004**, *3*, 115–120.